



THE UNIVERSITY *of* EDINBURGH

## Edinburgh Research Explorer

# Design and Evaluation of Wearable Multimodal RF Sensing System for Vascular Dementia Detection

### Citation for published version:

Anwar, U, Arslan, T, Hussain, A, Russ, TC & Lomax, P 2023, 'Design and Evaluation of Wearable Multimodal RF Sensing System for Vascular Dementia Detection', *IEEE Transactions on Biomedical Circuits and Systems*, pp. 1-14. <https://doi.org/10.1109/TBCAS.2023.3282350>

### Digital Object Identifier (DOI):

[10.1109/TBCAS.2023.3282350](https://doi.org/10.1109/TBCAS.2023.3282350)

### Link:

[Link to publication record in Edinburgh Research Explorer](#)

### Document Version:

Peer reviewed version

### Published In:

IEEE Transactions on Biomedical Circuits and Systems

### General rights

Copyright for the publications made accessible via the Edinburgh Research Explorer is retained by the author(s) and / or other copyright owners and it is a condition of accessing these publications that users recognise and abide by the legal requirements associated with these rights.

### Take down policy

The University of Edinburgh has made every reasonable effort to ensure that Edinburgh Research Explorer content complies with UK legislation. If you believe that the public display of this file breaches copyright please contact [openaccess@ed.ac.uk](mailto:openaccess@ed.ac.uk) providing details, and we will remove access to the work immediately and investigate your claim.



# Design and Evaluation of Wearable Multimodal RF Sensing System for Vascular Dementia Detection

Usman Anwar, Tughrul Arslan, Amir Hussain, *Senior Member, IEEE*, Tom C. Russ and Peter Lomax

**Abstract**—Vascular dementia is the second most common form of dementia and a leading cause of death. Brain stroke and brain atrophy are the major degenerative pathologies associated with vascular dementia. Timely detection of these progressive pathologies is critical to avoid brain damage. Brain imaging is an important diagnostic tool and determines future treatment options available to the patient. Traditional medical technologies are expensive, require extensive supervision and are not easily accessible. This paper presents a novel concept of low-complexity wearable sensing system for the detection of brain stroke and brain atrophy using RF sensors. This multimodal RF sensing system provides a first-of-its-kind RF sensing solution for the detection of cerebral blood density variations and blood clots at an initial stage of neurodegeneration. A customized microwave imaging algorithm is presented for the reconstruction of images in affected areas of the brain. Designs are validated using software simulations and hardware modeling. Fabricated sensors are experimentally validated and can effectively detect blood density variation ( $1050 \pm 50 \text{ Kg/m}^3$ ), artificial stroke targets with a volume of  $27 \text{ mm}^3$  and density of  $1025\text{-}1050 \text{ Kg/m}^3$ , and brain atrophy with a cavity of  $58 \text{ mm}^3$  within a realistic brain phantom. The safety of the proposed wearable RF sensing system is studied through the evaluation of the Specific Absorption Rate ( $\text{SAR} < 1.4 \text{ W/Kg}$ ,  $100\text{mW}$ ) and thermal conductivity of the brain ( $< 0.152 \text{ }^\circ\text{C}$ ). The results indicate that the device is viable as an efficient, portable, and low-cost substitute for vascular dementia detection.

**Index Terms**— Brain imaging, Microwave sensing system, Medical imaging, Multimodal sensing, Non-invasive sensors, Radio Frequency sensors, Ultra-wideband, Vascular dementia

## I. INTRODUCTION

Around one million people are living with a neurodegenerative disease in the UK. Neurodegenerative disease is strongly linked with age and the primary elements that lead to neurodegeneration include cognitive impairment, brain tumor, dementia, Alzheimer's disease (AD) and brain stroke [1].

This paper was submitted on January 20, 2023. This work was funded in part by U.K. Engineering and Physical Sciences Research Council (EPSRC) under Grant EP/T021063/1; and in part by the Higher Education Commission (HEC), Pakistan.

U. Anwar, T. Arslan and P. Lomax are with the School of Engineering, The University of Edinburgh, Edinburgh, United Kingdom (Email: [Usman.Anwar@ed.ac.uk](mailto:Usman.Anwar@ed.ac.uk), [Tughrul.Arsalan@ed.ac.uk](mailto:Tughrul.Arsalan@ed.ac.uk), [Peter.Lomax@ed.ac.uk](mailto:Peter.Lomax@ed.ac.uk)).

A. Hussain is with the School of Computing, Edinburgh Napier University, United Kingdom (Email: [A.Hussain@napier.ac.uk](mailto:A.Hussain@napier.ac.uk)).

Tom C. Russ is Director of the Alzheimer Scotland Dementia Research Centre at The University of Edinburgh, United Kingdom (Email: [T.C.Russ@ed.ac.uk](mailto:T.C.Russ@ed.ac.uk)).

Neurodegenerative diseases range from acute conditions like a stroke to progressive and degenerative conditions like vascular dementia. Cognitive impairment is an intermediate stage between minor neurodegeneration and severe diseases like dementia [2]. Other than the age factor, cognitive impairment is normally triggered by hypertension, diabetes, cardiovascular anomalies and hyperlipidemia. These underlying health conditions affect cerebral blood density which results in an increased risk of blood clots, stroke, hemorrhage, and neuronal damage. Early detection is important to slow down the neurodegenerative process and more severe decline to dementia. Delay in the diagnosis usually results in cognitive decline with progressive loss of brain neurons [3]. In some cases, it may lead to vascular dementia with an increased probability of brain stroke and brain hemorrhage.

Vascular dementia is the second most common form of dementia after Alzheimer's disease. Vascular dementia is usually triggered by decreased blood flow to the brain, either due to blood clots or cerebrovascular anomalies. The initial pathophysiological changes appear in the white matter of the brain. The increase in blood flow to the brain may result in a blood stroke or hemorrhage. In some cases, macro and micro-infarcts may develop due to blood clots, which lead to brain atrophy, cerebrovascular impairment, and a permanent condition of reduced blood flow to the brain [4]. The neurodegeneration that results from infarction and stroke is generally irreversible. A timely diagnosis is therefore critical to avoid the disease progression. Some medical imaging technologies, like Magnetic Resonance Imaging (MRI), Positron Emission Tomography (PET), and Computerized Tomography (CT), can detect neurodegeneration at advanced stages but require extensive medical supervision and are expensive. Brain MRI-based imaging can detect, monitor and quantify changes associated with microbleeds [5], white matter atrophy [6] and ischemic stroke [7]. A PET scan can be used to detect cerebral metabolism [8], stroke [9] and brain atrophy [10], but it requires injection of a radioactive tracer into the patient's blood. CT scan is a relatively fast, accurate and widely available imaging technique that is commonly used for stroke detection [11] and has a high sensitivity to visualize the blood vessels in the brain using CT angiography (CTA) [12]. Electroencephalogram (EEG) and magnetoencephalogram (MEG) are low-cost, widely available and non-invasive alternative to these traditional medical technologies. Although EEG and MEG can detect vascular cognitive impairment, but can only accurately sense brain activity at the surface level, which limits their sensitivity in

detecting early states of dementia [13], [14]. Along with an early dementia diagnosis, customized multimodal solutions like smart assistive living, mobility aids and cognitive stimulation therapy can effectively limit the progression of dementia [15]. Some recent studies have investigated dementia detection through commercial-grade wearable multimodal sensors like blood volume pulse, electrodermal activity, skin temperature and accelerometer sensor. Personalized machine learning models were developed to detect dementia based on behavioral symptoms and agitation biomarkers [16], [17]. This approach has limitations and necessitates synchronized multi-sensor data collection and large data set to validate the generalizability of machine learning algorithms.

Microwave sensing and imaging techniques provide a portable, flexible and low-exposure solution, which can substitute these traditional and off-the-shelf multimodal diagnostic technologies. Electromagnetic (EM) waves in the Ultra-wideband (UWB) frequency region are non-ionizing and can penetrate the skull, skin and tissues, which makes them ideal for diagnostic applications. In recent years, microwave sensing and imaging solutions have been developed for the detection of stroke, Alzheimer's disease and brain tumor. Vivaldi antenna array was proposed for the detection of stroke with multiple antenna elements interconnected using microwave coaxial switches [18]. A flexible 8-element monopole antenna array was presented for hemorrhagic stroke detection, operable at frequencies between 1.3 GHz and 3.5 GHz [19]. This device was suitable for wearable applications due to its flexible substrate material. A flexible electromagnetic cap with a 16-element antenna array was developed for brain stroke detection [20]. The antenna elements were integrated with a multilayer cap, and the device was validated by using stroke-mimicking targets in an artificial brain phantom. In another study, a three-dimensional (3D) electromagnetic head imaging system was presented for brain stroke diagnosis [21]. The designed 24-element planar antenna array was arranged in a dual elliptical ring configuration inside a compact flexible cap. A wearable hat-shaped device with integrated flexible microwave antennas was proposed to detect brain atrophy and lateral ventricle enlargement [22]. Brain atrophy was replicated on an artificial head phantom through an even reduction in white and grey matter volume and the replacement of gaps with cerebrospinal fluid. The wearable device was able to detect various degrees of brain atrophy and lateral ventricle enlargement in transmission and reflection modes.

Although the above-mentioned wearable RF technologies can detect neurodegeneration, most of them are designed for a specific neurodegenerative disease and require an array of antennas for the detection of those anomalies. However, this research work explores the multimodal detection of neurodegenerative and cerebrovascular anomalies through smart RF glasses. The portable sensing system operates with only two sensors and an unobtrusive design makes it an ideal product for a flexible healthcare system. The primary contributions of this work are as follows:

- This paper presents a customized meander line sensor with a low profile, high sensitivity and improved bandwidth. The enhanced gain is achieved through defected ground structure and optimization of the meander shape, width of the meander trace, and the number of meander sections.
- A novel crescent sensor is proposed with a compact structure evolved from a circular and donut-shaped monopole. The tapered feed line and slotted ground plane resulted in a high sensitivity, improved bandwidth and high impedance.
- This work demonstrates the detection and two-dimensional imaging of brain atrophy and stroke using a tailored microwave beamforming algorithm, which requires fewer sensors for full head coverage as compared to the literature.
- The imaging process is improved through multi-frequency imaging, as each sensor obtains images with higher resolution using microwave signals of different frequencies.

The rest of this paper is organized as follows: simulation and experimental methods are discussed in Section II. Section III presents an overview of the design and configuration of RF sensors. Section IV provides a detailed analysis of near-field software simulations for designed antenna sensors. The performance of a multimodal RF sensing system in an experimental setup is also investigated. An imaging algorithm is implemented for the reconstruction of two-dimensional brain images with atrophy and stroke. Future research direction along with considerations for improvement is discussed in Section V.

## II. METHODS

This paper presents the design, investigation and implementation of novel multimodal, wearable, low-cost, non-invasive and privacy-preserving smart Radio Frequency (RF) glasses for the detection of cerebral blood density, brain atrophy and brain stroke through the detection of major pathophysiological changes. Fig. 1 provides an insight into the design flow of the proposed sensing system. The novel concept of smart RF glasses is presented to make this device adaptable, conformable, and non-intrusive and to integrate it within the next generation of 5G and IoT-enabled hearing aid devices, as part of the COG-MHEAR project [23]. These multimodal hearing aid devices will be able to estimate the listening effort through embedded radiofrequency sensors, heart rate sensors, audio-visual cameras, context estimation, an eye tracker and a pupillometry sensor. Hearing loss may contribute to a fast progression of brain atrophy and mild hearing loss doubles the risk of developing dementia [24]. Therefore, the proposed RF sensing system will provide rapid detection and diagnosis for neurodegeneration that is associated with hearing loss. The RF sensors are integrated around the glasses to target, scan and monitor various areas of the brain. The integration of sensors around the glass frame helps to make the device non-invasive, conformable and

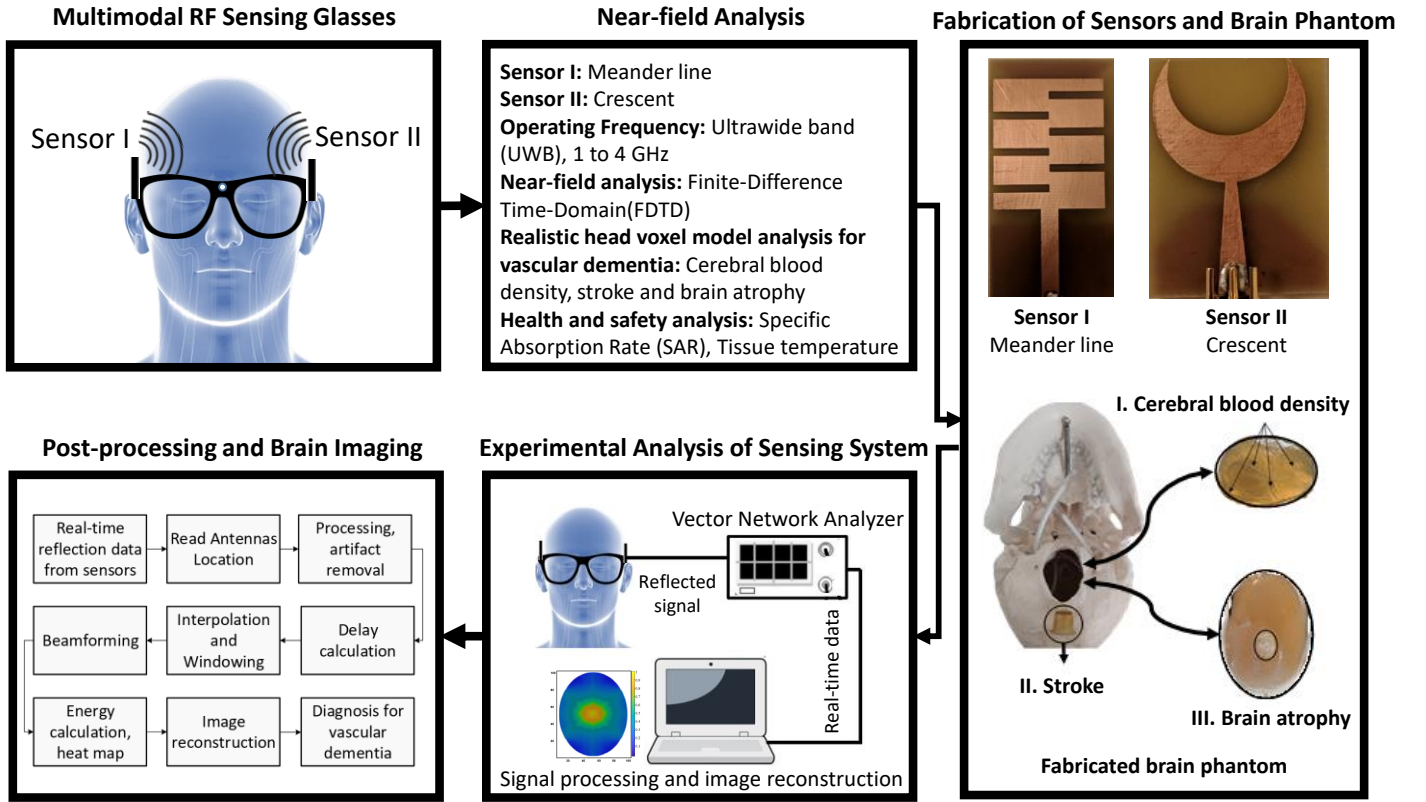


Fig. 1. Design flow of the proposed multimodal Radio Frequency (RF) sensing system

convenient for the elderly. This design also offers a minimalistic approach with two RF sensors attached to the side hinges of the glasses that are sufficient to scan the frontal, temporal and anterior parts of the brain. These RF sensors can detect the blood density variations in the middle cerebral, posterior cerebral, vertebral and internal carotid arteries that terminates at the circle of Willis junction. The proposed RF sensing system can also detect brain stroke and atrophy, which validates the multimodal detection capability of the embedded sensors.

In the first phase of this research, simulations were performed on CST Microwave Studio and two antenna sensors were designed for integration with the proposed RF glasses. Near-field analysis was performed to investigate the effectiveness of RF sensors in the detection of brain stroke, brain atrophy and blood density variations in the brain. Various computational brain models were designed to emulate these neurodegenerative conditions. To capture changes in various brain segments, RF glasses were placed near a head voxel model. In the second phase, RF sensors were fabricated and the artificial phantom was prepared using brain-mimicking material with the placement of artificial arteries, ventricles, atrophy and stroke targets. In the final phase of research, experiments were performed on fabricated realistic brain phantoms. Reflection data ( $S_{11}$ ) was gathered from sensors after each physical alteration in the fabricated phantom. Simulated and measured results were compared and analyzed to assess the integrity of obtained diagnosis. Health and safety parameters like Specific Absorption Rate (SAR)

and temperature of the target brain areas were analyzed to validate the safety of the wearable sensing system.

The reflection measurements ( $S_{11}$ ) taken from experimentation were processed to recreate images for both brain atrophy and stroke. To improve the imaging process, additional measurements were taken from the front and back of the head using a headband. This helped in an accurate reconstruction of images by ensuring complete coverage of brain phantom. The positioning of sensors remained the same on the RF glasses with the meander line sensor on the left and the crescent antenna on the right side of the glasses. The sensors on the headband are arranged by the placement of a meander line sensor on the front facing the forehead, and a crescent sensor facing the back of the head phantom.

### III. SENSOR DESIGN

To detect and diagnose cerebral blood density and vascular dementia degeneration, deep penetration into the head is required. The selection of operational frequency for the sensor is important to ensure maximum coverage inside the brain. The other important design parameters are the miniaturization and positioning of sensors around the brain. The antenna sensors presented in this research are designed to operate on an Ultra-wideband (UWB) frequency range, between 1 GHz and 4 GHz. This frequency band is selected to ensure maximum penetration and coverage inside the brain. Both antenna sensors are miniaturized to integrate with wearable glasses. The design of antenna sensors is novel and the sensors are capable of detecting cerebral blood density, atrophy and

stroke. The proposed sensors are optimized to provide unidirectional radiation. This helped to minimize the effects of nearby objects and resulted in efficient microwave power utilization. Antenna sensors are placed on the left and right hinges of glasses, with radiating patches facing the skin.

Meander line antenna is designed and miniaturized using multiple patches of the ground plane. The sensor provides good  $S_{11}$  performance at 1.2 GHz and 2.5 GHz. The proposed meander line sensor-I has dimensions of 30 x 60 mm<sup>2</sup> and is implemented on FR4 substrate with a dielectric constant of 4.4 and a thickness of 1.6 mm. The designed antenna contains a single monopole radiating element that is fed with a 50  $\Omega$  feed line, as depicted in Fig. 2. Width of the feeding line is  $F_W = 4$  mm and length is  $F_L = 24$  mm. A square-shaped partial ground plane at the bottom and an inverted triangular ground plane are introduced on top of the RF sensor structure to improve the bandwidth and reflection at lower frequencies. Other dimensions of the sensor are given in Table I.

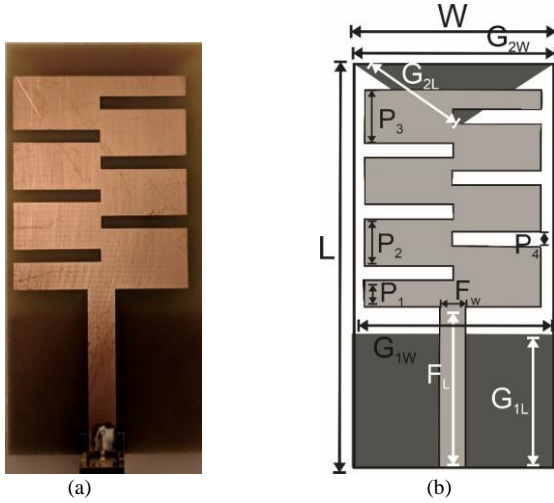


Fig. 2. (a) Fabricated meander line antenna sensor-I (b) Geometric configuration of meander line antenna sensor-I

A crescent-shaped antenna sensor is designed with a partial ground plane structure to improve the reflection at lower frequencies. The crescent shape of radiating element helps to maintain high impedance bandwidth and compact structure. Initially, a single-element Ultra-wideband (UWB) monopole antenna was designed and miniaturized using partial and defected ground structures. A circular patch was first implemented on CST Microwave Studio, but the  $S_{11}$  characteristics were not optimum, it was then modified to a donut-shaped monopole. The antenna was then transformed to a crescent shape by chamfering an inner circle from this donut-shaped monopole. The crescent shape helped to lower the resonant frequency of antenna sensors and resulted in a considerable improvement in bandwidth. The reflection results ( $S_{11}$ ) for the circular, donut-shaped monopole and final crescent shape sensor are presented in Fig 3. The resonant frequency of the antenna sensors can be approximately calculated using (1), where  $f_1$  is the resonant frequency,  $c$  is

the speed of light,  $\epsilon_r$  is the relative permittivity of the substrate and  $L$  is the side length of antenna structure [25].

$$f_1 = \frac{c}{L\sqrt{2(\epsilon_r + 1)}} \quad (1)$$

The geometry of the ground plane and radiating structure is altered to miniaturize the design for crescent antenna sensor-II, which has dimensions of 22 x 31 mm<sup>2</sup> and is designed on FR4 substrate with a dielectric constant of 4.4 and thickness of 1.6 mm. A single crescent-shaped monopole radiating element is designed on top of a chamfered ground plane that is fed with a 50  $\Omega$  triangular tapered feed line, as shown in Fig. 4. The length of feeding line is  $F_L = 14$  mm, width of feeding line near the radiating element and feed port is  $F_{W1} = 1$  mm and  $F_{W2} = 4$  mm respectively. The partial ground plane is chamfered from the upper edges, which resulted in bandwidth improvements for sensor-II. High impedance is achieved by tapering the feedline. The overall dimensions of sensor-II are listed in Table I.

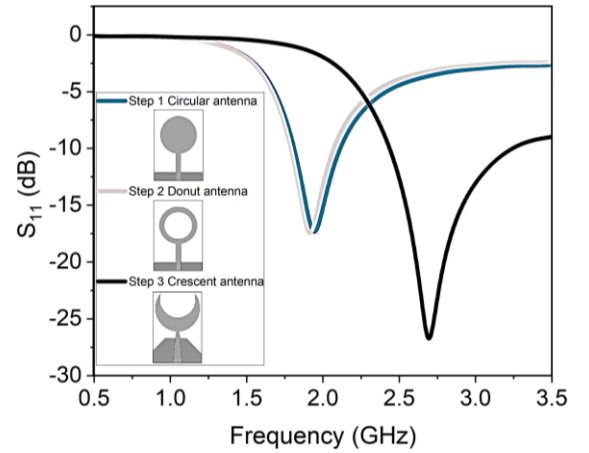


Fig. 3. Simulated reflection results ( $S_{11}$ ) at each design step of crescent antenna sensor-II

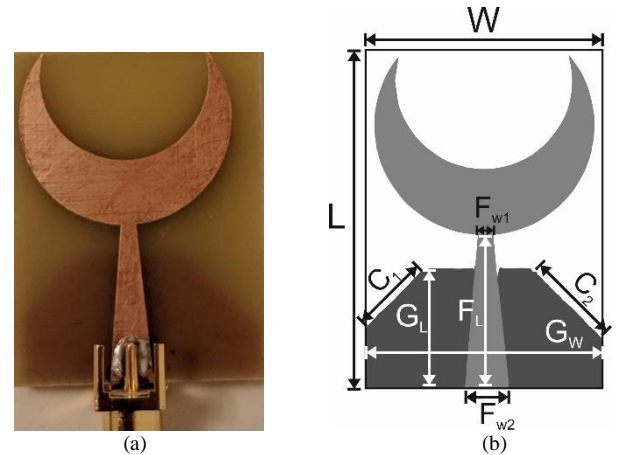


Fig. 4. (a) Fabricated crescent antenna sensor-II (b) Geometric configuration of crescent antenna sensor-II



TABLE I  
DIMENSIONS OF ANTENNA SENSORS

Meander line antenna		Crescent antenna	
Parameter	Dimensions (mm)	Parameter	Dimensions (mm)
Length (L)	60	Length (L)	31
Width (W)	30	Width (W)	22
Ground length, square ( $G_{1L}$ )	20	Ground length ( $G_L$ )	17
Ground length, triangle ( $G_{2L}$ )	10	Ground width ( $G_W$ )	22
Ground width, square ( $G_{1W}$ )	30	Feeding line length ( $F_L$ )	14
Ground width, triangle ( $G_{2W}$ )	30	Feeding line width near radiating element ( $F_{W1}$ )	1
Feeding line length ( $F_L$ )	24	Feeding line width near feed port ( $F_{W2}$ )	4
Feeding line width ( $F_W$ )	4	Ground left chamfer ( $C_1$ )	5.3
Meander line patch width ( $P_1$ )	4	Ground right chamfer ( $C_2$ )	7
Meander line patch width ( $P_2$ )	7		
Meander line patch width ( $P_3$ )	8		
Meander line patch width ( $P_4$ )	2		

#### IV. RESULTS

##### A. Simulation Results and Near-Field Analysis

Microwave sensing works on the basis of variations in reflected signal strength. The microwave signals are reflected differently based on these dielectric variances between healthy and diseased tissues. The dielectric changes in the targeted brain areas determine the blood and cerebrospinal fluid (CSF) concentration and density. The backscattered signals are then analyzed to determine the problematic area of the brain. The level of reflection determines the cause of neurodegeneration. Reflected signals aid in the identification of strokes, brain atrophy, white matter changes or lesions, protein deposits, micro and macro infarcts, and microbleeds.

CST Microwave Studio was used for the proposed work's near-field computational modeling and analysis. The sensors were first miniaturized by keeping the gain, directivity, Specific Absorption Rate (SAR) and other design parameters in an optimal range. The meander-line and crescent-shaped sensors were then simulated for sensing blood density variation, stroke, and brain atrophy. Meander line sensor-I and

crescent sensor-II were placed on the left and right sides of wearable glasses respectively, as shown in Fig. 5 (a). A realistic voxel model [26] is used for software simulations, with various brain entities like skull, skin, bones, grey matter, white matter, blood, cerebrospinal fluid, and ventricles. The cross-sectional view of brain entities along with the placement of RF sensors on wearable glasses is shown in Fig. 5 (b). During simulation, the properties of these individual brain segments were adjusted to simulate blood density, blood clots, and brain atrophy pathologies. Initial  $S_{11}$  measurements were recorded before any changes to the head voxel as a benchmark. The  $S_{11}$  simulated measurements were taken with an antenna-tissue spacing of 10 mm, 15 mm and 20 mm to assess the optimum antenna-tissue separation for both sensors. The results are presented in Fig. 6 (a-b), which indicate that the sensors can operate more effectively when placed 10 mm away from the brain.

Cerebral blood density was emulated using variations in the material density, conductivity and dielectric permittivity. The customized voxel model for cerebral blood density simulations is shown in Fig. 5 (c-d). For initial simulations, the actual blood density of  $1050 \text{ kg/m}^3$  was configured for the blood pool of the voxel model [27] [28]. Density was increased to  $1100 \text{ kg/m}^3$  for the moderately high case of cerebral blood density. For high blood density, the Rho value for material is changed to  $1150 \text{ kg/m}^3$ . In addition, for moderate and high blood densities, electrical conductivity was increased. For each sensor position, the reflection result ( $S_{11}$ ) is measured against the variation in blood density inside the brain voxel model. It can be seen in Fig. 6 (c-d) that there is a strong reflection and a higher downward shift in  $S_{11}$  for the high blood density state as compared to low and moderate blood density. This confirms that the sensors are working accurately for the detection of cerebral blood density variation.

For brain stroke and brain atrophy emulation, changes were made in the grey matter and white matter of the brain model. For brain atrophy simulations, the relative permittivity was reduced from 54.8 to 41 for grey matter and 40.5 to 36.5 for white matter. For stroke analysis, the permittivity of the blood pool was decreased from 63.2 to 56.5 and blood density was increased from  $1060 \text{ kg/m}^3$  to  $1190 \text{ kg/m}^3$ . The detail of changes made in the parameters for each brain entity is presented in Table II. The simulated reflection results ( $S_{11}$ ) for both brain atrophy and stroke are presented in Fig. 6 (e-f).

TABLE II  
VARIATION IN SIMULATED PARAMETERS FOR BRAIN ENTITIES

Simulated condition	Blood			Gray Matter			White Matter		
	Dielectric permittivity ( $\epsilon$ )	Material density ( $\rho$ )	Conductivity (S/m)	Dielectric permittivity ( $\epsilon$ )	Material density ( $\rho$ )	Conductivity (S/m)	Dielectric permittivity ( $\epsilon$ )	Material density ( $\rho$ )	Conductivity (S/m)
Normal brain	63.2	1050	1.38	54.8	1045	0.77	40.5	1041	0.47
Moderately high blood density	66	1100	1.46	54.8	1045	0.77	40.5	1041	0.47
High blood density	71	1150	1.55	54.8	1045	0.77	40.5	1041	0.47
Brain stroke	73	1190	1.55	54.8	1045	0.77	40.5	1041	0.47
Brain atrophy	63.2	1050	1.38	41	750	0.65	36.5	545	0.59

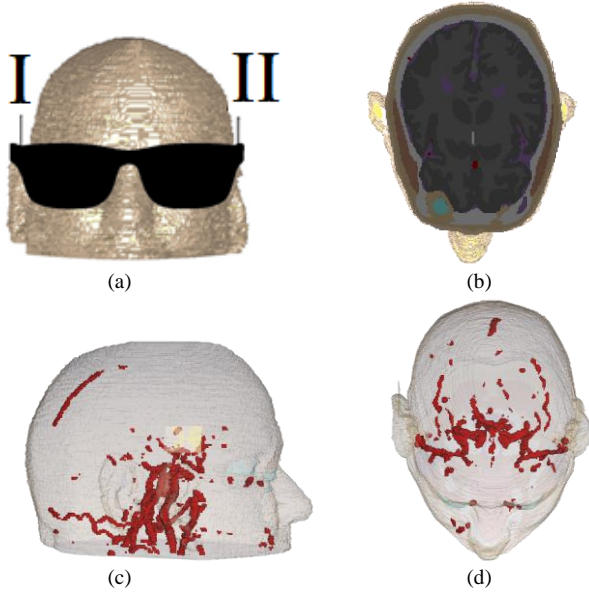


Fig. 5. Head voxel model used in software simulations with (a) RF sensors placed on glasses (b) Cross-sectional view of model from top with brain entities, veins and layers (c) Side view of voxel model with cerebral blood arteries (d) Top view of voxel model with blood arteries

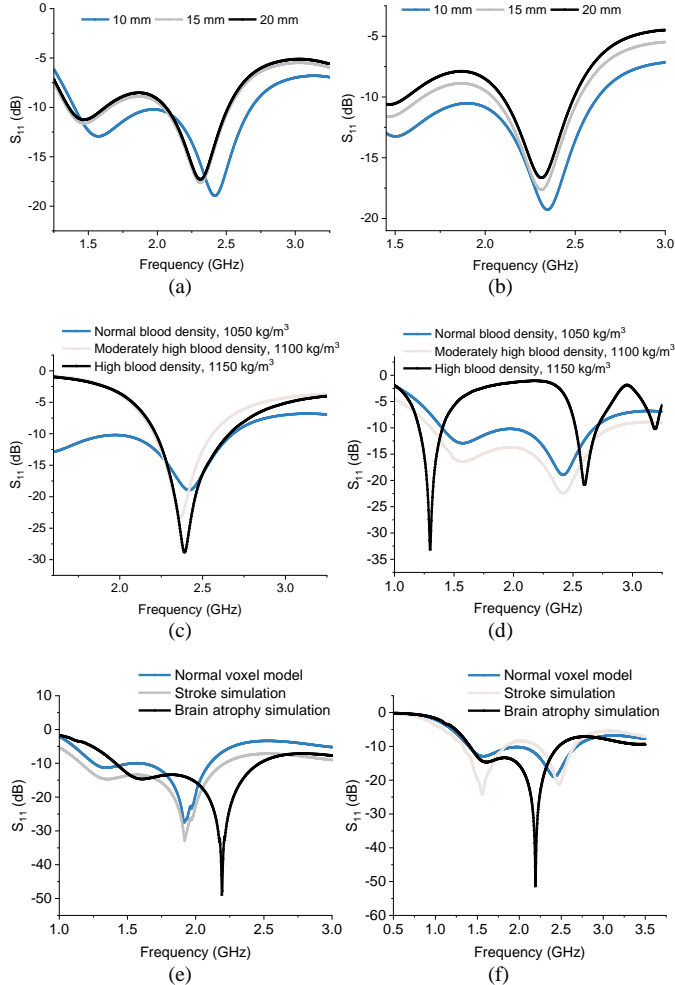


Fig. 6. Simulated reflection ( $S_{11}$ ) results (a) Meander line sensor-I antenna-tissue separation results with normal brain voxel (b) Crescent sensor-II antenna-tissue separation results with normal brain voxel (c) Cerebral blood density for meander line antenna sensor-I (d) Cerebral blood density for crescent antenna sensor-II (e) Stroke and brain atrophy for meander line antenna sensor-I (f) Stroke and brain atrophy for crescent antenna sensor-II

The performance of RF sensors was validated while operating in close proximity to the human head voxel. The time-domain characterization was carried out by radiating a pulse into the brain. Field probes were placed inside the voxel model at a distance of 30 mm and 60 mm from the sensors. The field strength and shape of the pulse travelling from the antenna towards brain voxel model are shown in Fig. 7 (a) and Fig. 7 (b) for sensor-I and sensor-II respectively. The E-field strength is reduced by half in case of sensor-I and by one-third in case of sensor-II. A considerable delay is observed in the pulse when operated near the head model, which is due to the impact of biological layers on the transmitted electromagnetic wave. The field probe results validate the selection of Ultra-wideband (UWB) frequencies for the proposed RF sensors. The directionality of the proposed RF sensors is evaluated by calculating front-to-back (F/B) ratio. This is the ratio of transmitted power and the reflected power. The simulated peak front-to-back ratio of sensor-I is 16 dB and sensor-II is 17 dB, as presented in Fig. 7 (c).

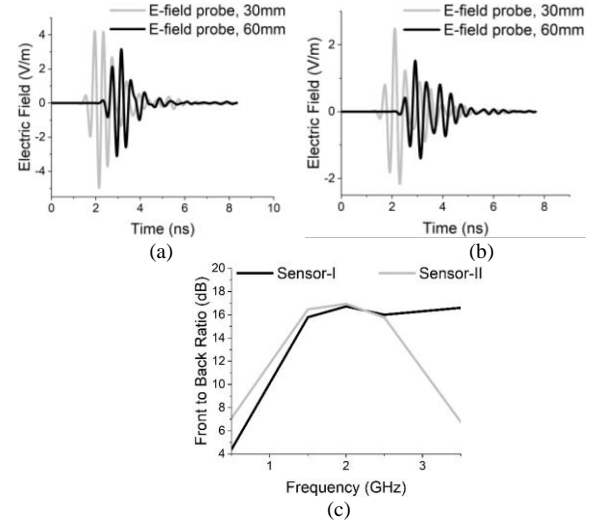


Fig. 7. Simulated near-field time-domain pulses at distance of 30 mm and 60 mm inside head phantom (a) Meander line antenna sensor-I (b) Crescent antenna sensor-II (c) Front-to-back ratio of sensors

The impact of using RF sensors on brain safety is crucial when they are operating within close proximity to the brain. The primary factor to measure this is the radiation intensity absorbed by the brain during exposure to RF sensors. This is calculated through the Specific Absorption Rate (SAR), which provides the safe amount of radiation absorbed by the body during exposure. International Commission for Non-Ionizing Radiation Protection (ICNIRP) permits a maximum of 2 W/Kg SAR per 10g of mass [29]. The maximum power

absorption for meander line sensor-I is 1.4 W/Kg for an input power of 100 mW, operating at 10 mm away from the brain voxel, as shown in Fig. 8 (c). For the crescent antenna sensor-II, the maximum value of SAR is 1.15 W/Kg for an input power of 100 mW, at 10mm from brain phantom, as presented in Fig. 8 (d). SAR values are calculated at different locations from the brain voxel model to monitor the variations. The measured SAR values for these simulations against the input power of 1 mW, 10 mW and 100 mW are given in Table III. All the SAR values are within a permissible range, which validates that the device is safe for medical diagnostic applications. SAR can be calculated for each antenna sensor using (2), where  $\sigma$  is the conductivity of the material,  $E$  is the electric field value and  $m_d$  is the mass density of the target human tissue [30].

$$SAR = \frac{\sigma \times E^2}{m_d} \quad (2)$$

Another important safety factor to consider is the impact of RF sensors on body temperature. The transient behavior of the temperature was measured on CST Studio Suite thermal transient solver. Thermal simulations provided the temperature status of all brain segments including skin, skull, gray and white matter. The default temperature of brain voxel model was configured as 36 °C and the overall influence of antenna sensors on the temperatures was studied. The maximum increase in temperature was observed for skin layer while the sensors were in operation, which was 36.152 °C for sensor-I and 36.144 °C for sensor-II. There was a minimal increase in temperature for the skull, white and gray matter and the average temperature rise is too small to have any adverse effect on the health and safety of the brain. The measured values of average temperature increase for brain entities are recorded in Table IV.

The amount of penetration inside the brain voxel model is determined through the E-field distribution. The penetration depth is evaluated for proposed RF sensors at a frequency of 1.5, 2 and 2.5 GHz, with an input power of 100 mW to the sensors. The maximum amount of penetration inside the brain for both sensors was at 2.5 GHz. While operating on this frequency, both sensors were able to reach the temporal and parietal lobes while propagating through white and grey matter, as shown in Fig. 8 (a-b). This counter-validates the efficacy of designed RF sensors in near-field operation.

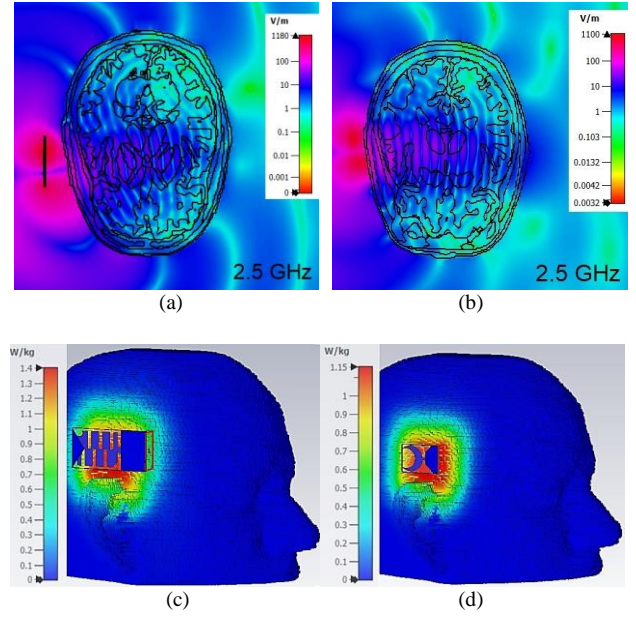


Fig. 8. Simulated E-field distribution of proposed antenna sensors inside the head (top-view) at 2.5 GHz (a) Meander line antenna sensor-I (b) Crescent antenna sensor-II; Simulated Specific Absorption Rate (SAR) for (c) Meander line antenna sensor-I at 2.5 GHz (d) Crescent antenna sensor-II at 2.5 GHz

### B. Experimental Results And Evaluation of Multimodal Sensing System

The simulated results were experimentally validated using the proposed RF glasses and fabricated head phantom. The measurements were taken using an artificial brain phantom with brain-mimicking material filled inside, representing grey and white matter. The fabricated antenna sensors were mounted on wearable glasses to make the device comfortable and convenient for the patients. Antenna sensors I and II are arranged on the side hinges of the glasses. The Sub Miniature version A (SMA) coaxial RF connectors are placed to the sides to accommodate the cables connecting sensors with the Vector Network Analyzer (VNA), which is being used to generate and monitor the reflected signal received by the sensors. HP 8753C VNA was used for experiments, which has a frequency range of 300 kHz to 3 GHz and a dynamic range of up to 100 dB. The experimental setup used to verify the designed system is shown in Fig. 9.

TABLE III  
SPECIFIC ABSORPTION RATE (SAR) OF ANTENNA SENSORS (PER 10G) WITH INPUT POWER (MILLIWATT)

Distance from Brain phantom (mm)	Sensor-I SAR (W/Kg)			Sensor-II SAR (W/Kg)		
	1 mW	10 mW	100 mW	1 mW	10 mW	100 mW
10	0.014	0.14	1.4	0.012	0.116	1.15
15	0.015	0.11	1.08	0.009	0.085	0.85
20	0.008	0.074	0.74	0.006	0.062	0.62



TABLE IV  
MAXIMUM TEMPERATURE RISE IN BRAIN AREAS (CELSIUS)

Simulated Sensor	Skin	Skull	Gray matter	White matter
Sensor-I	0.152	0.147	0.132	0.124
Sensor-II	0.144	0.138	0.12	0.115

The experimentation is done using RF sensors, VNA, a brain skull model and a personal computer with measurement software. VNA ports were calibrated first using open, short and load connectors. After calibration, both sensor-I and sensor-II were connected to the 50  $\Omega$  ports available on VNA using SMA wires. The output power from VNA to the antenna sensors was 1.25 mW for each port.  $S_{11}$  measurements were taken with RF glasses placed on an empty skull model, as a benchmark.

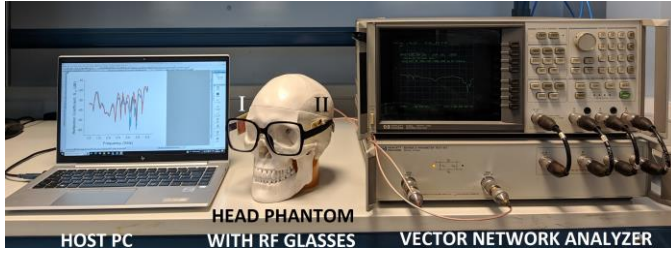


Fig. 9. Experimental setup with VNA, laptop, head phantom, and portable RF glasses.

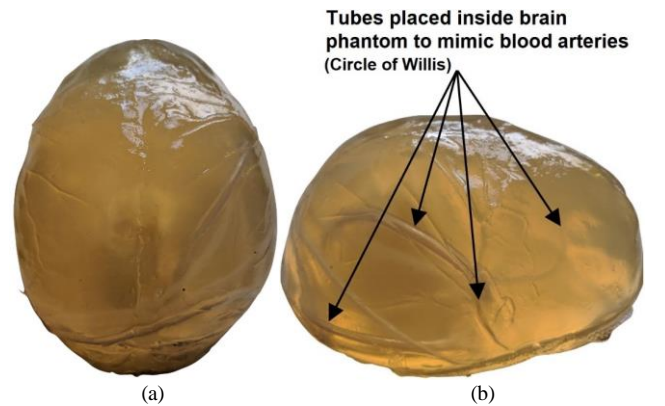
An artificial brain phantom is prepared [31] using the grey matter layer, white matter layer and the tubes placed inside the material to represent the blood vessels. For the preparation of grey and white matter layers, a mixture of water, sugar and agar is prepared with an overall concentration of 1400 ml to match the total brain volume of an average male. Since water has a high dielectric constant of 78.4, sugar was first dissolved in the water to lower the dielectric constant. Agar powder was added to the boiling mixture of water and sugar. The boiled liquid was then poured inside the skull model to solidify into a jelly-like material. The material composition of the brain phantom is given in Table V. Dielectric properties of the phantom mixture, blood-mimicking liquids and stroke targets were measured using two-port VNA HP8753C connected to Agilent high-temperature dielectric probe 85070E-0020. VNA was connected to a laptop PC using a General Purpose Interface Bus (GPIB) connector and software associated with the dielectric probe was used to capture dielectric properties. The dielectric values and density of the blood-mimicking liquids and stroke targets are given in Table VI.

TABLE V  
COMPOSITION OF BRAIN PHANTOM MIXTURE

Material	Quantity
Water	700 ml (700 g)
Sugar	600 ml (510 g)
Agar	100 ml (35 g)
Total Volume	1400 ml

The proposed RF glasses were verified on skull phantom with polyvinyl chloride (PVC) and silicone tubes placed inside to represent arteries. The tubes were placed in an arrangement to mimic the circle of Willis, which is an important junction of arteries at the base of the human brain. The experimentation involved measuring of blood density for two blood-mimicking liquids. Liquid-A was saline water that has the same properties as real blood, with a density of 1025 kg/m<sup>3</sup> and a dielectric constant of 66 [32]. Saline water was injected inside these tubes to mimic blood within major arteries. The experimentation was initiated with sensors placement around a normal brain phantom and a reference dataset for the proposed model was collected first with low-density liquid-A inside the brain phantom. The tubes were then filled with a high-density liquid-B to observe the effect of blood density variation inside the brain. Liquid-B was pure milk with a density of 1050 kg/m<sup>3</sup> and a dielectric constant of 71 [33]. Reflection measurements ( $S_{11}$ ) were taken from both sensors along the temporal and frontal parts of the brain for low and high-density blood-mimicking liquids. The results are presented in Fig. 11 (a-b); there is a strong reflection in the case of high-density liquid-B with a high dielectric constant. This indicates an increased loss in the signal for high-density blood-mimicking liquid when measured with sensor-I and sensor-II. The experimentation results indicate that the designed antenna sensors can accurately detect the density of blood mimicking liquid inside the artificial cerebral arterial network. The proactive detection of blood density through RF sensing can help to reduce and prevent the risk of stroke, tissue and organ damage at a preliminary stage.

For stroke analysis, the proposed RF sensing system was first verified on a normal brain phantom placed inside the skull model. Reflection measurements ( $S_{11}$ ) were taken using both RF sensors and were kept as a reference benchmark when there was no anomaly. This reference dataset was helpful in the reconstruction of images for both experimental cases of vascular dementia: brain atrophy and stroke. The artificial stroke target-A was emulated using a shallow spherical target with a volume of 27 mm<sup>3</sup> [32], as shown in Fig. 10 (c). This spherical ischemic stroke target-A was filled with saline liquid to match the dielectric constant of an actual blood clot. The target was placed in the middle of the brain phantom to create an artificial brain stroke scenario.



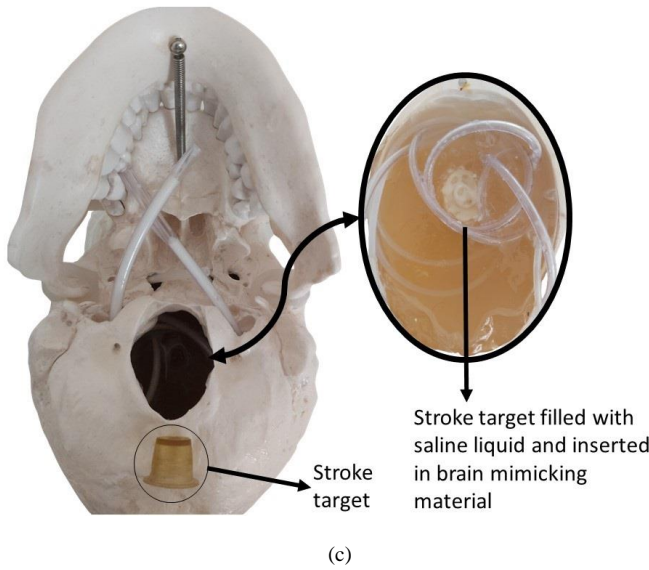


Fig. 10. (a) Fabricated gel-based brain phantom (b) Gel-based brain phantom for cognitive load emulation (c) Fabricated brain phantom with stroke target

Reflection measurements ( $S_{11}$ ) were taken with RF glasses placed around the head phantom. There is a strong reflection in the presence of stroke target-A compared to the normal brain, as shown in Fig. 11 (c-d).  $S_{11}$  measurements were taken with another stroke target-B to have a comparison between the reflection performance. This stroke target-B was filled with a mixture of coconut oil and pure milk [33]. This stroke object has a higher density of  $1050 \text{ Kg/m}^3$  compared to the actual blood plasma which has a density of  $1025 \text{ kg/m}^3$ . The dielectric constant of the mixture added to stroke target-B is relatively higher as compared to the actual blood, as given in Table VI. The S-parameters indicate a higher loss for stroke target-B for both meander line and crescent sensors, as shown in Fig. 11 (c-d). The measured results confirm that the proposed RF sensing system is able to detect stroke and transient ischemic stroke.

TABLE VI  
DENSITY OF BLOOD MIMICKING LIQUIDS AND STROKE TARGETS USED IN EXPERIMENTS

Material	Density ( $\text{kg/m}^3$ )	Dielectric constant
Liquid-A (saline water)	1025	66
Liquid-B (pure milk)	1050	71
Stroke Target-A (saline)	1025	66
Stroke Target-B (mixture of coconut oil and milk)	1050	73

To emulate the brain atrophy scenario, the same brain phantom was modified through the removal of the stroke target and the creation of a cavity with a volume of  $58 \text{ mm}^3$  in the middle of brain matter [22]. The cavity was filled with a mixture of salt, agar and water to represent the cerebrospinal fluid (CSF) accumulation inside. The dielectric properties of this mixture were verified first to match it with the dielectric

values of CSF. The results were then taken with RF glasses and a clear reflection from CSF can be seen in Fig. 11 (e-f). The experimental results confirm that the proposed system is capable of detecting cerebral blood density, stroke and brain atrophy in the brain.

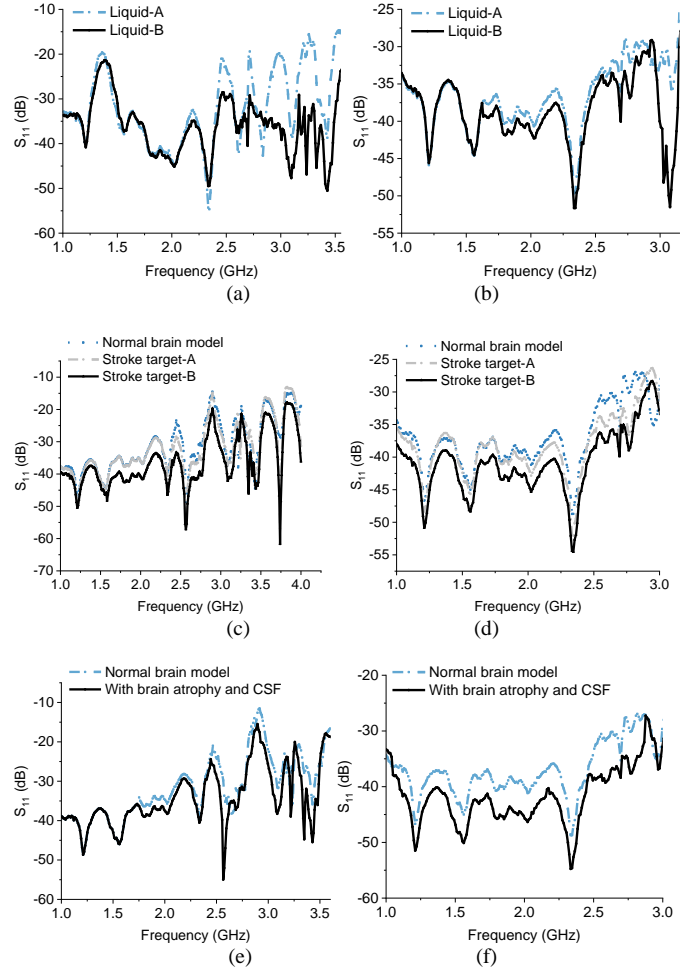


Fig. 11. Measured reflection ( $S_{11}$ ) results for (a) Cerebral blood density detection with meander line antenna sensor-I (b) Cerebral blood density detection with crescent antenna sensor-II (c) Stroke targets with meander line antenna sensor-I (d) Stroke targets with crescent antenna sensor-II (e) Brain atrophy and CSF with meander line antenna sensor-I (f) Brain atrophy and CSF with crescent antenna sensor-II

The measured results are consistent with the simulated results and both sensors provide improved reflection ( $S_{11}$ ) results in the experimental setup, as shown in Fig. 12 (a-b). The crescent antenna sensor-II provides better simulation and measurement results for the detection of cerebral blood density variations, stroke and brain atrophy. In addition to this, the crescent antenna sensor-II is more compact ( $22 \times 31 \text{ mm}^2$ ), as compared to the meander line antenna sensor-I ( $30 \times 60 \text{ mm}^2$ ). This allows an easier integration for sensor-II within the proposed RF glasses. Furthermore, the crescent sensor-II has a lower Specific Absorption Rate (SAR) and results in minimal temperature increase for skin, skull, gray and white matter.

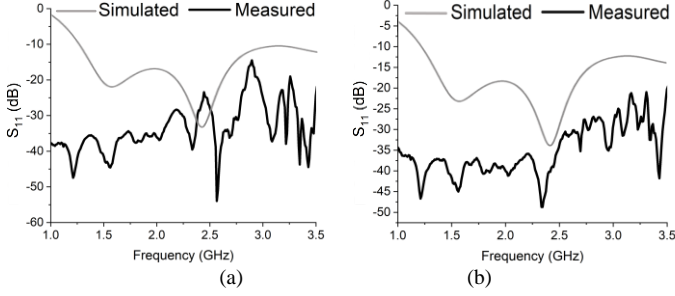


Fig. 12. Comparison of simulated and measured reflection ( $S_{11}$ ) results with normal brain phantom (a) Meander line antenna sensor-I (b) Crescent antenna sensor-II

### C. Imaging Of Stroke And Brain Atrophy

The imaging for stroke and brain atrophy is performed using Microwave imaging via a space-time (MIST) beamforming algorithm. The MIST algorithm uses energy levels of backscattered signals to reconstruct the image of malignant anomalies. The MIST algorithm implemented in this work is a modified improved version of the algorithm for breast cancer detection [34]. The results of the imaging algorithm are enhanced by using an average of reflection ( $S_{11}$ ) data sets collected from each sensor. The significant change in dielectric properties between the malignant part of the brain results in high levels of backscattered energy levels. The reflection data received through backscattering by the Ultra-wideband (UWB) antenna sensors is recorded to initiate the image processing. This dataset was used as an initial input to the imaging algorithm implemented in MATLAB. The received reflection data is converted from frequency to time domain using Inverse Fast Fourier Transform (IFFT) and is time-aligned through finite-impulse response (FIR) filters. The resultant signals are processed through time shifts, gating to remove the artifact and align the processed signals. The energy is calculated for each pixel of these resultant signals and stored in an image matrix. This image matrix is then compared with the reference image matrix of a normal brain phantom. The subtraction of two matrices provides an energy map of the malignant anomalies in case of stroke and brain atrophy. The flowchart of the MIST algorithm process is shown in Fig. 13.

The reflection measurements ( $S_{11}$ ) were first taken with a normal brain phantom as a reference dataset. The  $S_{11}$  values were normalized to compute the phase and magnitude of each signal. The imaging algorithm was implemented on the dataset obtained through the stroke target-A, stroke target-B and brain atrophy. The volume of each stroke target was 27 mm<sup>3</sup> and the dielectric properties of the stroke targets are given in Table VI. For stroke, the affected area is visible in the middle of the heat map which represents the spherical stroke target placed around the middle of the brain phantom. It can be noticed in Fig. 14 (d-e) that the variation in density of the stroke object is resulting in a high-intensity heat map for stroke target-B. The brain atrophy region is relatively more spread out due to the

wider cavity of 58 mm<sup>3</sup>, with red boundaries indicating the atrophy and yellow color representing the cerebrospinal fluid. The antennas were placed at the coordinates of (50, 0), (50, 100), (0, 50), (100, 50) according to the axis in Fig. 14. The reconstructed images are compared with the actual brain atrophy and stroke changes in the realistic phantom, as shown in Fig. 14.

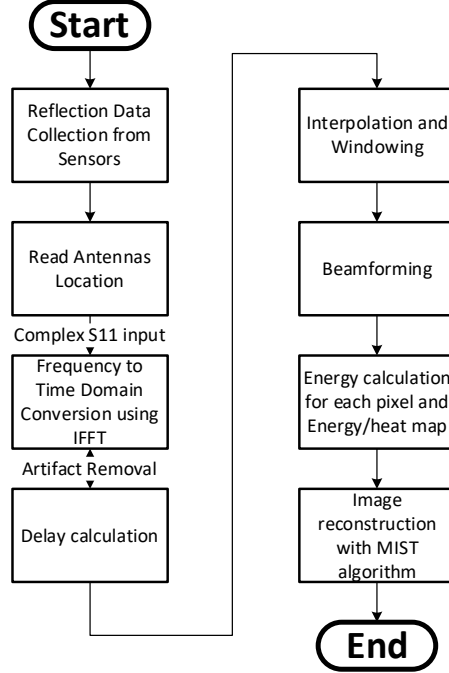


Fig. 13. Microwave Imaging in Space-Time (MIST) algorithm process flowchart

The image reconstruction is accurate in terms of the atrophy and stroke target location. The backscattered signal was normalized for both stroke brain atrophy measurements, as shown in Fig. 15. It can be observed that the reflection in the case of brain atrophy is higher as compared to the stroke in terms of magnitude (dB). Future work will be done to optimize it further to obtain the exact dimension of the malignant target. The image quality and contrast can also be improved through delay and sum (DAS) [35], [36], delay multiply and sum (DMAS) [37]–[39] and channel-ranked delay and sum (CR-DAS) [40], [41] algorithms.

In comparison with the relevant state-of-the-art work, the proposed multimodal RF sensing system provides the following advantages:

- The suggested system is cost-effective, non-invasive, unobtrusive, wearable, and requires minimal supervision, compared to conventional imaging technologies [8], [10], [11].
- In contrast to the proposed concept of miniaturized sensors embedded in RF glasses, the existing radiofrequency sensing techniques are relatively complex and less conformable with head-mounted sensor arrays [20], [21].



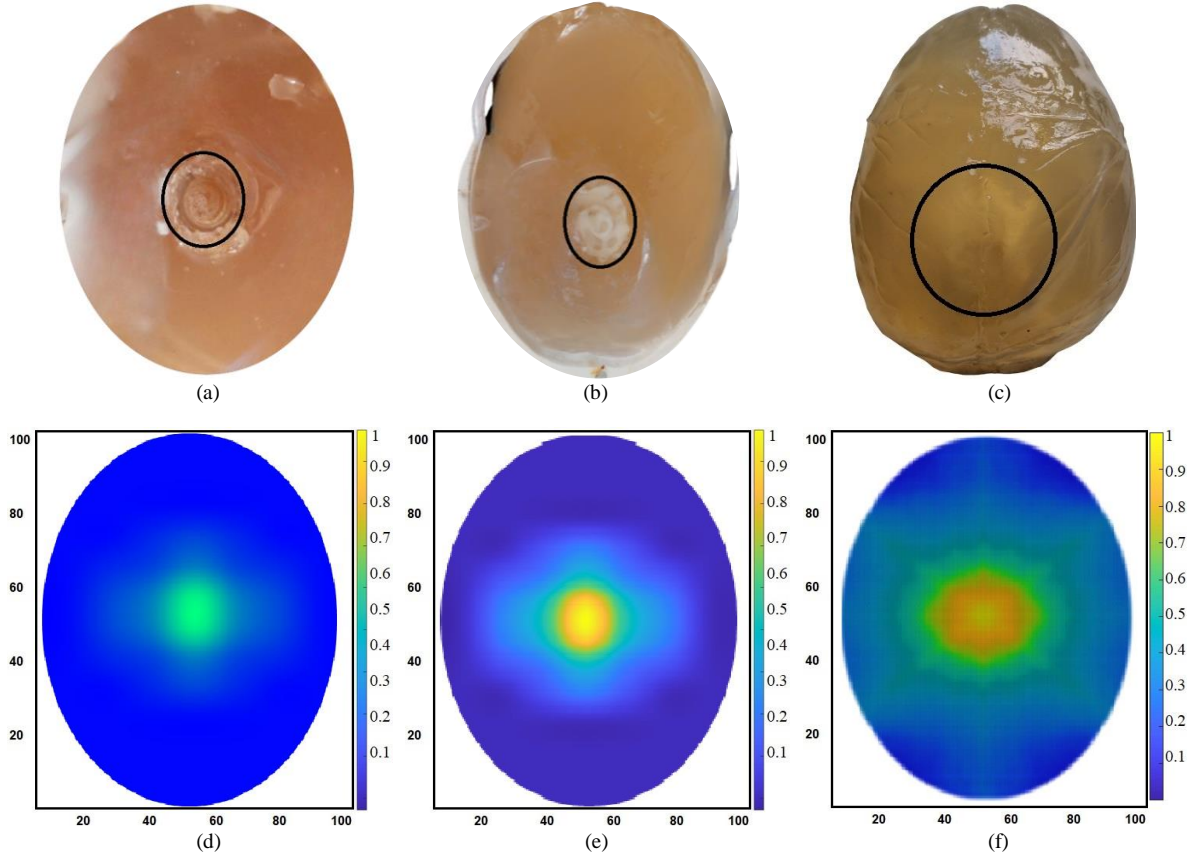


Fig. 14. Images of realistic brain phantom with (a) ischemic 27 mm<sup>3</sup> stroke target-A (b) ischemic 27 mm<sup>3</sup> stroke target-B (c) brain atrophy, 58 mm<sup>3</sup> cavity filled with CSF-mimicking liquid; and Reconstructed images using MIST beamforming algorithm for (d) ischemic stroke target-A (e) ischemic stroke target-B (f) brain atrophy

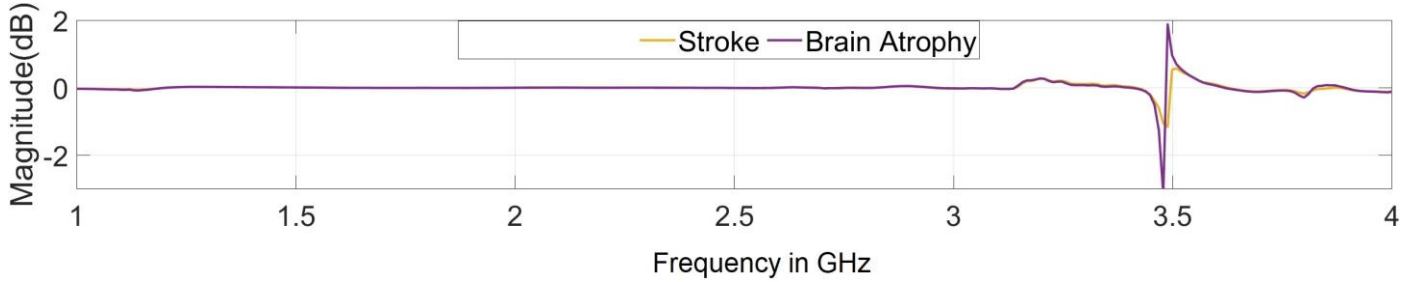


Fig. 15. Normalized backscattered signals for ischemic stroke target and brain atrophy (magnitude, dB)

- Our experiments validate the multi-modal detection capability of this RF sensing system. Existing solutions are designed for a single modality, either stroke [18], [19], [20], [21] or brain atrophy detection [22]. However, our proposed system detects multiple neurodegenerative anomalies with the same sensors.
- Our research is the first to investigate cerebral blood density detection using customized non-invasive RF sensors.
- The proposed sensing system ensures multimodal neurodegeneration detection with low sensor count, as compared to the existing radiofrequency techniques that involve multi-element antenna arrays (8, 16 or 24 elements) for brain sensing [19], [20], [21], [22].
- The proposed meander line and crescent sensors, when integrated within wearable RF glasses, can effectively operate with a high sensitivity to the antenna-tissue separation while maintaining safety features such as thermal effect on tissues and Specific Absorption Rate (SAR).

## V. CONCLUSION

A portable and wearable radio frequency system is developed for vascular dementia detection. The sensing system is capable of identifying brain atrophy, stroke and blood density variation in the brain at an initial stage. The design of sensors is optimized and miniaturized using computational software. The sensors are integrated with wearable smart glasses, and experimental validation of sensors has been performed by developing a realistic head phantom. Experimental results indicate that the designed sensors were able to detect the major pathophysiological anomalies associated with vascular dementia, like cerebral blood density, brain atrophy and stroke. The portable, cost-effective, user-centric and non-invasive design makes it a novel sensing system for medical diagnostic applications. Simulated and measured  $S_{11}$  results have confirmed that the device is capable of detecting variations in blood density inside the brain effectively. The measured results from the sensing system are post-processed using an enhanced microwave beamforming algorithm. The imaging algorithm accurately reconstructed the brain atrophy and stroke changes in the realistic phantom. The promising results confirm the capability of this portable and wearable imaging system for the early detection of neurodegeneration.

Future research will focus on the integration of this system with Internet of Things (IoT) sensors for real-time data transmission and processing that would be useful for robust remote sensing and imaging. The portable RF sensing system can be integrated with audio-visual sensors to enable emotion and cognition-aware neurodegeneration monitoring. The prospect of using flexible substrates for antennas can make future devices more conformable, resilient and manageable. A portable nano-VNA can be integrated into the wearable sensing system to make the device cost-effective and portable. The integration of 3D imaging algorithms can significantly accelerate the imaging reconstruction process and can improve accuracy and diagnosis. Another area that needs improvement is the development of 3D-printed lifelong phantoms with a more realistic representation of brain tissues, grey matter, white matter, skin, and blood pool.

## ACKNOWLEDGMENT

The authors like to thank Higher Education Commission, Pakistan and U.K. Engineering and Physical Sciences Research Council (EPSRC) supported COG-MHEAR project for funding this research. The authors would like to thank Dr. Rahmat Ullah for his guidance on the microwave imaging process. We are grateful to Mr. Iain Gold for his support and assistance in antenna fabrication.

## REFERENCES

- [1] M. M. Gonzales, V. R. Garbarino, E. Pollet, J. P. Palavicini, D. L. Kellogg, E. Kraig, and M. E. Orr, "Biological aging processes underlying cognitive decline and neurodegenerative disease," *The Journal of Clinical Investigation*, 16-May-2022. [Online]. Available: <https://www.jci.org/articles/view/158453>. [Accessed: 20-Mar-2023].
- [2] B. Christa Maree Stephan, T. Minett, E. Pagett, M. Siervo, C. Brayne, and I. G. McKeith, "Diagnosing mild cognitive impairment (MCI) in clinical trials: A systematic review," *BMJ Open*, vol. 3, no. 2, pp. 1–8, 2013, doi: 10.1136/bmjopen-2012-001909.
- [3] J. Rasmussen and H. Langerman, "Alzheimer's Disease – Why We Need Early Diagnosis," *Degener. Neurol. Neuromuscul. Dis.*, vol. 9, pp. 123–130, 2019, doi: 10.2147/DNND.S228939.
- [4] A. Brodtmann, M. S. Khelif, N. Egorova, M. Veldsman, L. J. Bird, and E. Werden, "Dynamic Regional Brain Atrophy Rates in the First Year after Ischemic Stroke," *Stroke*, no. September, pp. 183–192, 2020, doi: 10.1161/STROKEAHA.120.030256.
- [5] T. Saito *et al.*, "Cerebral Microbleeds Remain for Nine Years: A Prospective Study with Yearly Magnetic Resonance Imaging," *J. Stroke Cerebrovasc. Dis.*, vol. 27, no. 2, pp. 315–320, 2018, doi: 10.1016/j.jstrokecerebrovasdis.2017.09.001.
- [6] R. A. Feis *et al.*, "Multimodal MRI of grey matter, white matter, and functional connectivity in cognitively healthy mutation carriers at risk for frontotemporal dementia and Alzheimer's disease," *BMC Neurol.*, vol. 19, no. 1, pp. 1–11, 2019, doi: 10.1186/s12883-019-1567-0.
- [7] H. Cabral Frade, S. E. Wilson, A. Beckwith, and W. J. Powers, "Comparison of Outcomes of Ischemic Stroke Initially Imaged With Cranial Computed Tomography Alone vs Computed Tomography Plus Magnetic Resonance Imaging," *JAMA Netw. Open*, vol. 5, no. 7, p. E2219416, 2022, doi: 10.1001/jamanetworkopen.2022.19416.
- [8] J. Delrieu *et al.*, "The impact of a multi-domain intervention on cerebral glucose metabolism: analysis from the randomized ancillary FDG PET MAPT trial," *Alzheimer's Res. Ther.*, vol. 12, no. 1, pp. 1–11, 2020, doi: 10.1186/s13195-020-00683-6.
- [9] W. D. Heiss and O. Z. Weber, "Validation of MRI determination of the penumbra by PET measurements in ischemic stroke," *J. Nucl. Med.*, vol. 58, no. 2, pp. 187–193, 2017, doi: 10.2967/jnumed.116.185975.
- [10] W. D. Heiss, G. A. Rosenberg, A. Thiel, R. Berlot, and J. de Reuck, "Neuroimaging in vascular cognitive impairment: A state-of-the-art review," *BMC Med.*, vol. 14, no. 1, pp. 1–8, 2016, doi: 10.1186/s12916-016-0725-0.
- [11] C. A. Potter, A. S. Vagal, M. Goyal, D. B. Nunez, T. M. Leslie-Mazwi, and M. H. Lev, "Ct for treatment selection in acute ischemic stroke: A code stroke primer," *Radiographics*, vol. 39, no. 6, pp. 1717–1738, 2019, doi: 10.1148/rg.2019190142.
- [12] K. Murayama *et al.*, "Visualization of lenticulostriate arteries on CT angiography using ultra-high-resolution CT compared with conventional-detector CT," *Am. J. Neuroradiol.*, vol. 41, no. 2, pp. 219–223, 2020, doi: 10.3174/ajnr.A6377.
- [13] L. Torres-Simón, S. Doval, A. Nebreda, S. J. Llinas, E. B. Marsh,



- and F. Maestú, "Understanding brain function in vascular cognitive impairment and dementia with EEG and MEG: A systematic review," *NeuroImage Clin.*, vol. 35, no. January, 2022, doi: 10.1016/j.nicl.2022.103040.
- [14] F. Li *et al.*, "Predictive Diagnostic Approach to Dementia and Dementia Subtypes Using Wireless and Mobile Electroencephalography: A Pilot Study," *Bioelectricity*, vol. 4, no. 1, pp. 3–11, 2022, doi: 10.1089/bioe.2021.0030.
- [15] M. Zamiri *et al.*, "Review of technology-supported multimodal solutions for people with dementia," *Sensors*, vol. 21, no. 14, 2021, doi: 10.3390/s21144806.
- [16] A. Iaboni *et al.*, "Wearable multimodal sensors for the detection of behavioral and psychological symptoms of dementia using personalized machine learning models," *Alzheimer's Dement. Diagnosis, Assess. Dis. Monit.*, vol. 14, no. 1, pp. 1–11, 2022, doi: 10.1002/dad2.12305.
- [17] S. Spasojevic *et al.*, "A Pilot Study to Detect Agitation in People Living with Dementia Using Multi-Modal Sensors," *J. Healthc. Informatics Res.*, vol. 5, no. 3, pp. 342–358, 2021, doi: 10.1007/s41666-021-00095-7.
- [18] B. J. Mohammed, A. M. Abbosh, S. Mustafa, and D. Ireland, "Microwave system for head imaging," *IEEE Trans. Instrum. Meas.*, vol. 63, no. 1, pp. 117–123, 2014, doi: 10.1109/TIM.2013.2277562.
- [19] M. S. R. Bashri, T. Arslan, and W. Zhou, "Flexible antenna array for wearable head imaging system," *2017 11th Eur. Conf. Antennas Propagation, EUCAP 2017*, pp. 172–176, 2017, doi: 10.23919/EuCAP.2017.7928757.
- [20] A. S. M. Alqadami, A. Trakic, A. E. Stancombe, B. Mohammed, K. Bialkowski, and A. Abbosh, "Flexible Electromagnetic Cap for Head Imaging," *IEEE Trans. Biomed. Circuits Syst.*, vol. 14, no. 5, pp. 1097–1107, 2020, doi: 10.1109/TBCAS.2020.3025341.
- [21] A. Alqadami, A. Zamani, A. Trakic, and A. Abbosh, "Flexible Electromagnetic Cap for Three-Dimensional Electromagnetic Head Imaging," *IEEE Trans. Biomed. Eng.*, vol. 68, no. 9, pp. 2880–2891, 2021, doi: 10.1109/TBME.2021.3084313.
- [22] I. M. Saied and T. Arslan, "Noninvasive Wearable RF Device Towards Monitoring Brain Atrophy and Lateral Ventricle Enlargement," *IEEE J. Electromagn. RF Microwaves Med. Biol.*, vol. 4, no. 1, pp. 61–68, 2020, doi: 10.1109/JERM.2019.2926163.
- [23] *EPSRC COG-MHEAR Research Program*. Accessed: Mar. 2023. [Online]. Available: <http://cogmhear.org>
- [24] U. Anwar, T. Arslan, A. Hussain, and P. Lomax, "Next Generation Cognition-Aware Hearing Aid Devices With Microwave Sensors: Opportunities and Challenges," *IEEE Access*, vol. 10, no. July, pp. 82214–82235, 2022, doi: 10.1109/ACCESS.2022.3195875.
- [25] C. A. Balanis, *Antenna Theory: Analysis and Design*, 4th ed. New York, USA: John Wiley & Sons, Inc., 2016.
- [26] A. Arayeshnia, A. Keshtkar, and S. Amiri, "Realistic human head voxel model for brain microwave imaging," *2017 25th Iran. Conf. Electr. Eng. ICEE 2017*, pp. 1660–1663, 2017, doi: 10.1109/IranianCEE.2017.7985315.
- [27] B. Thomas and K. S. Sumam, "Blood Flow in Human Arterial System-A Review," *Procedia Technol.*, vol. 24, pp. 339–346, 2016, doi: 10.1016/j.protcy.2016.05.045.
- [28] E. Soleimani, M. Mokhtari-Dizaji, N. Fatourae, and H. Saberi, "Assessing the blood pressure waveform of the carotid artery using an ultrasound image processing method," *Ultrasonography*, vol. 36, no. 2, pp. 144–152, 2017, doi: 10.14366/usg.16019.
- [29] G. Ziegelberger *et al.*, "Guidelines for limiting exposure to electromagnetic fields (100 kHz to 300 GHz)," vol. 118, no. 5, pp. 483–524, 2020, doi: 10.1097/HP.0000000000001210.
- [30] J. W. Hand, R. W. Lau, J. J. W. Lagendijk, J. Ling, M. Burl, and I. R. Young, "Electromagnetic and thermal modeling of SAR and temperature fields in tissue due to an RF decoupling coil," *Magn. Reson. Med.*, vol. 42, no. 1, pp. 183–192, 1999, doi: 10.1002/(SICI)1522-2594(199907)42:1<183::AID-MRM24>3.0.CO;2-I.
- [31] S. Candefjord *et al.*, "Microwave technology for detecting traumatic intracranial bleedings: tests on phantom of subdural hematoma and numerical simulations," *Med. Biol. Eng. Comput.*, vol. 55, no. 8, pp. 1177–1188, 2017, doi: 10.1007/s11517-016-1578-6.
- [32] M. S. R. Bashri and T. Arslan, "Low-cost and compact RF switching system for wearable microwave head imaging with performance verification on artificial head phantom," *IET Microwaves, Antennas Propag.*, vol. 12, no. 5, pp. 706–711, 2018, doi: 10.1049/iet-map.2017.0486.
- [33] T. K. Kataria, A. Corona-Chávez, J. L. Olvera-Cervantes, R. Rojas-Laguna, and M. E. Sosa-Morales, "Dielectric characterization of raw and packed soy milks from 0.5 to 20 GHz at temperatures from 20 to 70 °C," *J. Food Sci. Technol.*, vol. 55, no. 8, pp. 3119–3126, 2018, doi: 10.1007/s13197-018-3238-3.
- [34] E. J. Bond, X. Li, S. C. Hagness, and B. D. Van Veen, "Microwave imaging via space-time beamforming for early detection of breast cancer," *IEEE Trans. Antennas Propag.*, vol. 51, no. 8, pp. 1690–1705, 2003, doi: 10.1109/TAP.2003.815446.
- [35] S. A. Shah Karam, D. O'Loughlin, B. L. Oliveira, M. O'Halloran, and B. M. Asl, "Weighted delay-and-sum beamformer for breast cancer detection using microwave imaging," *Measurement*, vol. 177, no. August 2020, p. 109283, 2021, doi: 10.1016/j.measurement.2021.109283.
- [36] M. Klemm, I. J. Craddock, J. A. Leendertz, A. Preece, and R. Benjamin, "Improved Delay-and-Sum Beamforming Algorithm for Breast Cancer Detection," *Int. J. Antennas Propag.*, vol. 2008, pp. 1–9, 2008, doi: 10.1155/2008/761402.
- [37] R. Ullah and T. Arslan, "Parallel delay multiply and sum algorithm for microwave medical imaging using spark big data framework," *Algorithms*, vol. 14, no. 5, 2021, doi: 10.3390/a14050157.
- [38] M. T. Islam, T. Islam, and S. Kibria, "Microwave Breast Imaging Using Compressed Sensing Approach of Iteratively Corrected Delay Multiply and Sum Beamforming," *Diagnostics*, vol. 11, pp. 1–12, 2021, doi: 10.3390/diagnostics11030470.
- [39] S. A. S. Karamfard and B. M. Asl, "Fast Delay-Multiply-and-Sum Beamformer: Application to Confocal Microwave Imaging," *IEEE Antennas Wirel. Propag. Lett.*, vol. 19, no. 1, pp. 14–18, 2020, doi: 10.1109/LAWP.2019.2951575.

- [40] M. O. Halloran, M. Glavin, and E. Jones, "Improved CMI Beamforming Algorithm," pp. 0–3, 2011, doi: 10.1109/URSIGASS.2011.6051375
- [41] M. A. Elahi *et al.*, "Evaluation of image reconstruction algorithms for confocal microwave imaging: Application to patient data," *Sensors (Switzerland)*, vol. 18, no. 6, 2018, doi: 10.3390/s18061678.



**USMAN ANWAR** received his B.S. in electrical (telecommunication) engineering from the National University of Computer and Emerging Sciences (NUCES), FAST, Islamabad, Pakistan in 2010 and his M.S. in telecommunication engineering from the University of Engineering and Technology, Taxila, Pakistan in 2016. He is currently pursuing his Ph.D. at the School of Engineering, The University of Edinburgh, Edinburgh, U.K. with a research focus on neurodegeneration detection through RF and microwave sensors.

His research interests include microwave and millimeter-wave antennas, Ultra-wideband MIMO and flexible biomedical sensors. He has an experience of over 10 years in the telecommunication industry; he worked as an Assistant Manager at Pakistan Telecommunication Company Limited from 2011 to 2016 and as Manager from 2016 to 2021 in the same organization.



**TUGHRUL ARSLAN** holds the Chair of Integrated Electronic Systems with the School of Engineering, The University of Edinburgh, Edinburgh, U.K. He is a member of the Integrated Micro and Nano Systems (IMNS) Institute and leads the Embedded Mobile and Wireless Sensor Systems (EWireless) Group with the University ([ewireless.eng.ed.ac.uk](http://ewireless.eng.ed.ac.uk)). His research interests include developing low-power radio frequency sensors for wearable and portable biomedical applications. He is the author of more than 500

refereed papers and inventor of more than 20 patents.

Prof. Arslan is currently an Associate Editor for the IEEE Transactions on VLSI Systems and was previously an Associate Editor for the IEEE Transactions on Circuits and Systems I (2005–2006) and IEEE Transactions on Circuits and Systems II (2008–2009). He is also a member of the IEEE CAS Executive Committee on VLSI Systems and Applications (1999 to date), and a member of the steering and technical committees of several international conferences. He is a co-founder of the NASA/ESA Conference on Adaptive Hardware and Systems (AHS) and currently serves as a member of its steering committee.



**AMIR HUSSAIN** received the B.Eng. and Ph.D. degrees in electronic and electrical engineering from the University of Strathclyde, Glasgow, U.K., in 1992 and 1997, respectively.

Following post-doctoral and senior academic positions at the University of the West of Scotland, Paisley, U.K., from 1996 to 1998, the University of Dundee, Dundee, U.K., from 1998 to 2000, and the University of Stirling, Stirling, U.K., from 2000 to 2018, respectively, he joined Edinburgh Napier University, Edinburgh, U.K., as

the Founding Head of the Cognitive Big Data and Cybersecurity (CogBiD) Research Laboratory and the Centre for AI and Data Science. His research interests include cognitive computation, machine learning, and computer vision. He has (co)authored several patents and over 500 publications, including 250+ journal papers and 20+ Books/monographs. He has led major national and international projects, including the current (\$4 Million) EPSRC funded COG-MHEAR grant and supervised over 35 PhD students. He is currently Chapter Chair of the Industry Applications Society, and (founding) Vice-Chair for the IEEE CIS Task Force on Intelligence Systems for e-Health.



**TOM RUSS** is a Consultant Psychiatrist and Honorary Clinical Reader at the Centre for Clinical Brain Science, Division of Psychiatry at The University of Edinburgh, Edinburgh, U.K. He is the Director of the Alzheimer Scotland Dementia Research Centre. He trained in medicine and psychiatry in Edinburgh, the Highlands and London and work clinically with older people with functional mental illness and dementia. He is the secretary of the Royal College of Psychiatrists in Scotland philosophy and psychiatry special interest group and sits on the Working with Older People steering group at Human Development Scotland (formerly the Scottish Institute of Human Relations).



**PETER LOMAX** holds the position of Senior Experimental Officer at The University of Edinburgh, Edinburgh, U.K., managing the Scottish Microelectronics Centre within the school of Integrated Micro and Nano Systems (IMNS). Involved principally in research projects involving micro and nano fabrication technologies.

He has 24 years of industrial and academic experience, ranging from Radio Operator on an Antarctic research base to Principal

Investigator (PI) on research projects. His research areas include X-ray emitter fabrication and MEMS/Nano detectors.